ADVANCED MATERIALS
www.advmat.de

Carbonized Silk Fabric for Ultrastretchable, Highly Sensitive, and Wearable Strain Sensors

*Chunya Wang, Xiang Li, Enlai Gao, Muqiang Jian, Kailun Xia, Qi Wang, Zhiping Xu, Tianling Ren, and Yingying Zhang**

Electronics with flexible, stretchable, and wearable features have risen exponentially to be next-generation electronics.[1–8] Wearable strain sensors, as an important subfield of wearable electronics, should be mechanically compliant and be able to conform to natural motions, so as to monitor human activities and personal health.[9] However, conventional strain-sensing platforms based on semiconductors and metal foils could not fulfill the requirements of wearable strain sensors because of their rigidity, low resolution, and low sensing range (usually <5%).[10,11] Various attempts have been made to develop flexible and wearable strain sensors by using nanomaterials as sensing elements coupled with elastic polymers as flexible, stretchable, and durable support materials. Nanomaterials, such as silicon nanoribbons,[12] metal nanoparticles or nanowires,[13,14] and low-dimensional carbons (e.g., carbon nanotubes (CNTs),[15–20] graphene,[21–27] and carbon blacks[28]), have been widely utilized because of their outstanding electrical and mechanical properties. Especially, carbon nanomaterials, for their remarkable flexibility, have drawn great attention for their potential utilization as sensing elements[29,30] or as conductive fillers[31] in flexible strain sensors. Nonetheless, vast majority of the reported sensors could not simultaneously attain high sensitivity (indicated by gauge factor (GF)) and high stretchability (indicated by tolerable strain), which limits their applications in monitoring full-range human motions. For example, a previous work[26] showed a graphene-based strain sensor, which had an ultrahigh GF up to 1000 but very limited strain range of 0–2%, restricting its applications in monitoring large deformations. On the contrary, another work[19] reported an extremely elastic strain sensor based on dry-spun CNT fibers which could be stretched by over 900%. Unfortunately, it exhibited a GF of only 0.54 in the strain range of 0–400%, limiting its applications in detecting subtle deformations of a human body induced by pulse, respiration, facial expression, and phonation. Very recently, a graphene-based fiber strain sensor[25] was reported for its high sensitivity and relatively wide workable strain range (up to 100%), which is still not enough for detecting motions induced by multiple joints which are usually larger than 100%.[19] Thus, the development of flexible strain sensors with both of high sensitivity and ultrahigh stretchability remains a big challenge.

Compared to CNTs and graphene, carbon-based materials from natural biomaterials have received extensive research interests owing to their good electrical conductivity, large-scale, and low-cost production capability as well as environmental benignity.[32] Silk, as a kind of widely used ancient natural material, is composed of sericin and fibroin, among which fibroin is the major component and consists of repetitive crystalline heavy chains (forming discrete β-sheet crystallites) and non-crystalline light chains (forming amorphous domains).[33,34] Silk fibroin has been reported to transform into graphitic nanocarbon by thermal treatment because of the fact that the β-sheet crystallites in the silk polypeptides could be aromatized or cyclized into sp^2-hybridized carbon structure.[35] It has been reported that carbonized silkworm cocoon or regenerated silk fibroin, based on their good electrical conductivity, showed good performance for energy conversion and storage.[36–41] We surmised that carbonized silk fibers, based on their unique carbon nanoplate structures, might work as strain sensors with high sensitivity. On the other aspect, silk fibers (tens of microns in diameter) derived from Bombyx mori, with the advantages of outstanding mechanical performance, high resilience, lustrous appearance, and large-scale production,[42,43] have been widely applied in the textile industry for thousands of years. Commercially available silk fabrics, including woven fabrics and knitted fabrics, generally show hierarchical structures composed of yarns consisting of parallel or twisted silk fibers. This unique structures provide possibility to achieve good stretchability. However, to the best of our knowledge, the application of carbonized silk fabrics (CSFs) or other natural fiber fabrics for sensors has not been explored.

In this work, we demonstrated for the first time that CSFs could be used for the fabrication of ultrastretchable and highly sensitive strain sensors, which showed superior performance in detecting both large and subtle human motions. Particularly, the CSF-based strain sensor which had a plain-weave structure, where the weft yarns were composed of parallel fibers and the warp yarns were composed of twisted fibers, showed combined

C. Y. Wang, M. Q. Jian, K. L. Xia, Q. Wang, Prof. Y. Y. Zhang
Department of Chemistry and Center for Nano and Micro Mechanics (CNMM)
Tsinghua University
Beijing 100084, P. R. China
E-mail: yingyingzhang@tsinghua.edu.cn
X. Li, Prof. T. L. Ren
Institute of Microelectronics and Tsinghua National Laboratory for Information Science and Technology (TNList)
Tsinghua University
Beijing 100084, P. R. China
E. L. Gao, Prof. Z. P. Xu
Center for Nano and Micro Mechanic (CNMM)
School of Aerospace Engineering
Tsinghua University
Beijing 100084, P. R. China

DOI: 10.1002/adma.201601572

superiority of wide sensing range (from 0% to more than 500% strain), high sensitivity, fast response (<70 ms), and high durability (10 000 cycles), indicating its great potential for application in wearable devices and intelligent robots. Noted that it is the first time utilizing the hierarchical structure of carbonized woven fabrics for applications in strain sensors and flexible electronics. The concept could be readily extended to other woven fabrics, such as cotton, modal, and other fabrics, paving a new way for the low cost and scalable fabrication of wearable strain sensors.

Figure 1a illustrates the structure of a pristine silk fabric and the fabrication process of CSF strain sensors. Here, we use a plain-weave silk fabric, which showed the best performance according to our results, as an example. The pristine silk fabric was carbonized through thermal treatment under an inert atmosphere (see the Experimental Section for details). To fabricate strain sensors, the CSFs were encapsulated with an elastic silicone named Ecoflex. As shown in Figure 1a, the warp yarns in this structure are composed of twisted silk fibers, while the weft yarns are composed of parallel silk fibers. Each silk fiber is composed of millions of silk fibroin molecules, which assembles in two main structures: the amorphous domain structure and the β-sheet crystallite structure. Particularly, the β-sheet crystallite structure contains two or more protein strands which are stabilized by numbers of hydrogen bonds between the proximal peptide chains. During the structure reconstruction induced by heat treatment, the intermolecular dehydration between the adjacent peptide chains may result in aromatization or cyclization, leading to the formation of hexagonal carbon rings or even highly ordered graphitic structures.[35] As shown in Figure 1b,c, after carbonization, the area of the silk fabric shrunk to 41.9% of the original one, while the morphology was kept very well. Figure 1d,e show the optical images of the pristine silk fabric and the carbonized fabric, illustrating the well maintained plain-weave structure of the fabric after carbonization. Figure 1f–h shows the remarkable robustness of the strain sensors, which kept good electrical conductivity while being twisted or knotted.

Figure 2a shows a typical scanning electron microscopy (SEM) image of a carbonized plain-weave silk fabric, revealing the well reserved woven structures from the pristine silk fabric, in which the weft yarns (x-direction) are composed of

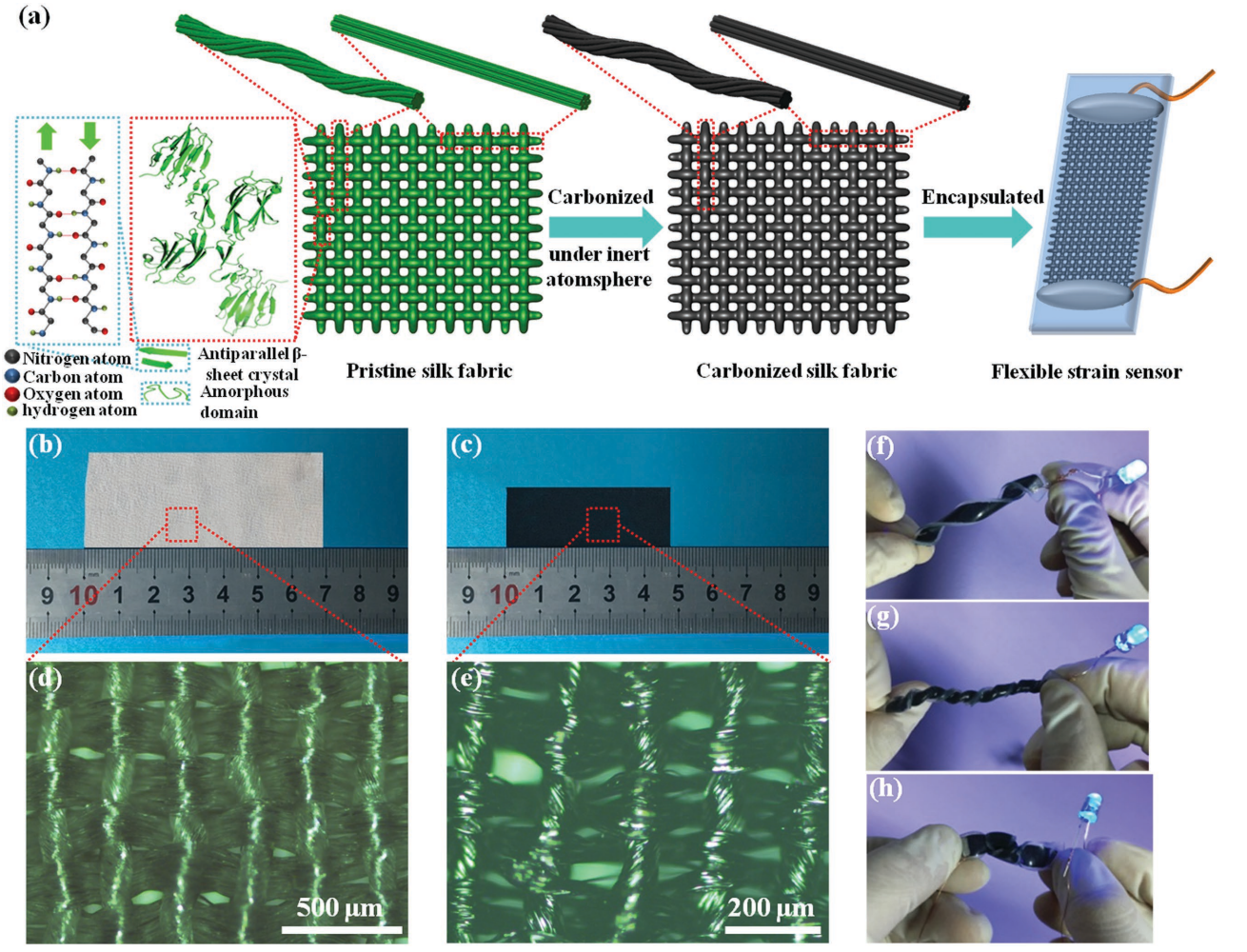

Figure 1. Extremely stretchable CSF strain sensor. a) Illustration showing the hierarchical structures and the fabrication of CSF strain sensors. A plain-weave structure is used as an example. Photographs and enlarged optical images of (b,d) a pristine plain-weave silk fabric and (c,e) the corresponding carbonized silk fabric. f–h) Photographs of a strain sensor connected with a light-emitting diode, showing its robustness while being twisted or knotted.

Adv. Mater. **2016**,
DOI: 10.1002/adma.201601572

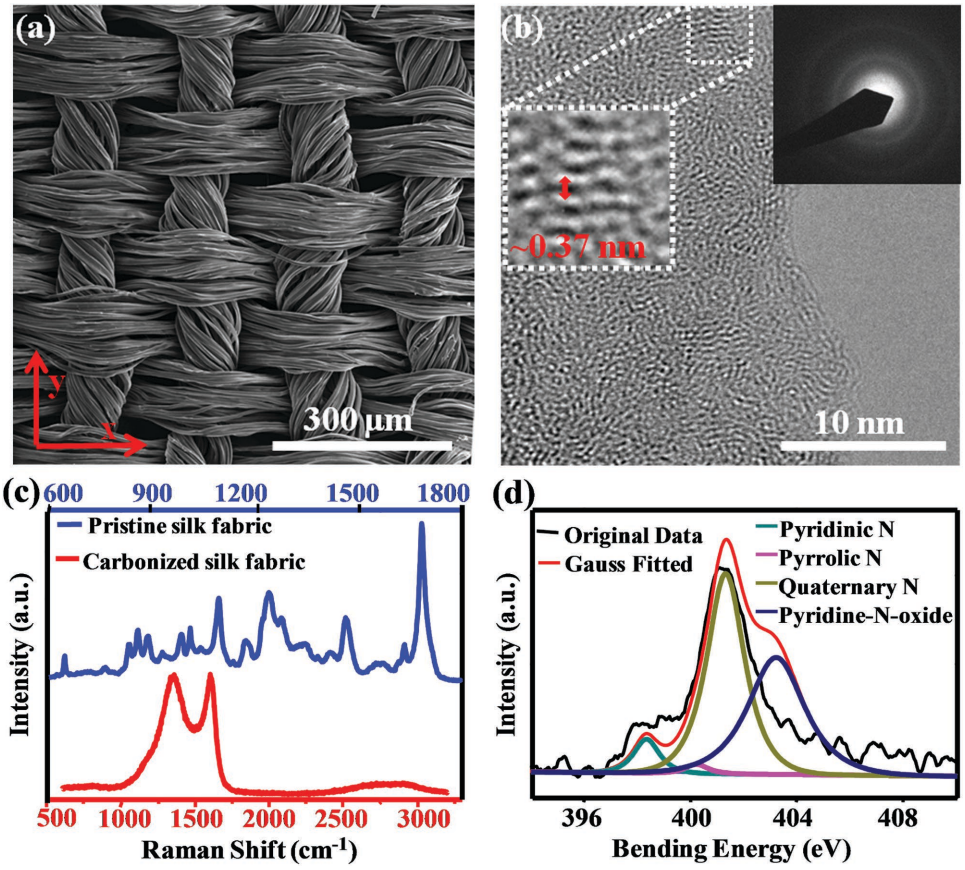

Figure 2. Characterization of carbonized silk fabric. a,b) SEM and TEM images of the carbonized silk fabric. c) Raman spectra of the pristine and carbonized silk fabric. d) XPS spectrum showing the N 1s peak of the carbonized silk fabric.

parallel fibers and the warp yarns (y-direction) are composed of twisted fibers (see SEM image of the pristine silk fabric in Figure S1a, Supporting Information). As shown in Figure 2b, a typical transmission electron microscope (TEM) image of the carbonized silk fibroin displays distorted lattice fringes with an interlayer spacing of 0.37 nm, which belongs to the interplanar spacing of the (002) plane for hexagonal graphite.[44] The slight expanded interplanar spacing is related to the doping of N and O, which has been confirmed by energy-dispersive X-ray spectroscopy mapping (Figure S1b–e, Supporting Information). The Raman spectrum of the CSF (Figure 2c) presents a G-band at 1593 cm^{-1} (associated with crystalline sp^2 carbon) and a D-band at 1352 cm^{-1} (related to defects or heteroatom doping). The existence of a relatively broad and weak 2D band (around 2750 cm^{-1}) in the Raman spectrum also reveals the defective or heteroatom doped nanographene nature of the carbonized silk. Besides, the Raman spectrum of the pristine silk fabric shows feature peaks of silk fibroin at 832, 856, 884, 1086, 1230, 1265, and 1667 cm^{-1}. The high and sharp peak at 1667 cm^{-1}, which belongs to the amide I band, indicates the high content of β-sheet crystallites,[45] which is beneficial for the formation of graphitic nanocarbon in the process of thermal treatment.[35]

X-ray photoelectron spectroscopy (XPS) measurement was performed to further ascertain the chemical state of the heteroatoms in the carbonized silk. The XPS survey spectra of the pristine and CSF confirm the presence of C, N, and O elements (Figure S2a, Supporting Information). Elemental analysis from XPS measurements further reveals the content of C, N, O in carbonized silk are 91.2%, 2.7%, and 6.1%, respectively, compared to 62.6%, 17.0%, and 20.4% in pristine silk (see Table S1, Supporting Information). As shown in Figure 2d (Supporting Information), the N1s spectrum of the CSF can be fitted by four peaks at 398.3 eV (attributed to pyridinic N), 400.2 eV (attributed to pyrrolic N), 401.4 eV (attributed to quaternary or graphitic N), and 403.2 eV (attributed to pyridine-N-oxide N), indicating the transformation of part of *N* elements within the silk into *N* substituents in graphene or graphite layers, which contributes to the good electrical conductivity of the obtained carbonized silk.[46] The C 1s spectrum also demonstrates the presence of C—N bond (Figure S2b, Supporting Information). The relatively high graphitized structure and the intrinsic N-doping endows the CSF with excellent electrical conductivity (≈140 Ω sq^{-1}), which is essential for applications in low power consumption strain sensors.

The strain sensors made from the plain-weave CSF showed high sensitivity with tolerable strain up to 520%. **Figure 3**a shows photographs of the pristine and the stretched strain sensor. The strain was applied in y direction of the plain-weave structure. Figure 3b shows a typical plot of relative change in resistance versus strain of the CSF strain sensors, where R_0 and R represent the pristine resistance and the real-time resistance when being stretched, respectively. The CSF strain sensor

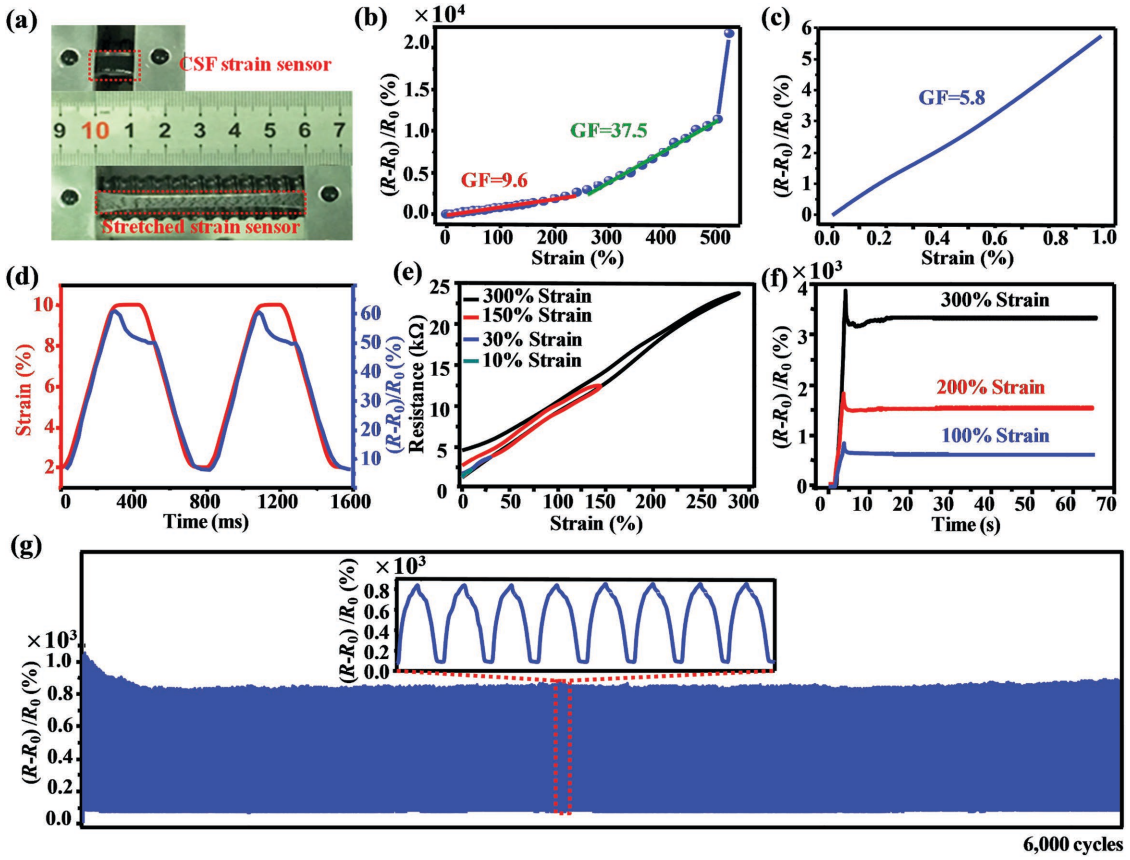

Figure 3. Electromechanical properties of the CSF strain sensor. a) Photograph of the pristine and stretched CSF strain sensor, showing its ultraelasticity. b) Relative change in resistance of the strain sensor versus the applied strain in the *y*-direction (strain rate 30% min^{-1}). c) Resistance variation versus strain within strain range of 0–1%. d) Relative change in resistance (blue) for cycling between 2% and 10% strain (red) at 1.25 Hz, showing the fast response of the sensor. e) Resistance for different strain during the loading–unloading cycle, showing the hysteresis of the sensor. f) Relative change in resistance for a step strain from 0% to 100% (blue), 200% (red), and 300% (black) (strain rate 40% s^{-1}), showing the low creep of the strain sensor. g) Relative change in resistance under repeated loading and unloading of 100% strain for 6000 cycles, showing the durability of the sensor.

displays a monotonic increase in resistance with a maximal strain up to 520% at which point the sensor failed. The plot could be divided into two linear regions with different slopes, corresponding two GFs. The GF is 9.6 for strain range within 250% and 37.5 for 250–500%, demonstrating the ultraelasticity and high sensitivity of the CSF strain sensor. Particularly, the ultraelastic CSF strain sensor shows a GF of 5.8 even for very small strain in the range of 0–1% (Figure 3c), which is almost three times of that of the conventional metal gauge (2.0).[47] The high sensitivity at both small and large strain, as well as the extremely large sensing range enable the CSF strain sensors to monitor and recognize full-range human activities.

Besides, CSF strain sensors with other woven structures, such as twill-weave, satin-weave and interlock-stitch, were also fabricated and investigated (Figure S3, Supporting Information). The twill-weave and satin-weave silk fabric based sensors also exhibited high sensitivity and large tolerable strain of more than 300% when being stretched in the *y*-direction (Figure S4a,b, Supporting Information). For the twill-weave CSF strain sensor, GF is 4.0 and 22.1 in the strain range within 200% and 200–350%, respectively, and for satin-weave CSF strain sensor, GF is 5.2 and 15.0 with the strain range within 100% and 100–280%, respectively. In contrast, the interlock-stitch CSF strain sensors showed a maximal strain less than 75% when being stretched in both x and y directions (Figure S4c,d, Supporting Information). We can conclude that, among all the investigated CSF strain sensors with different woven structures, the sensors with plain-weave structures show both of the highest sensitivity as well as the largest elasticity.

Furthermore, we found that the plain-weave CSF strain sensors exhibited fast response, low creep, and high durability. The relative resistance changes of the CSF strain sensor for cyclic loading in the strain range of 2–10% at a frequency of 1.25 Hz obviously revealed the immediate response of the sensor to external strain (Figure 3d). Note that the shape mismatch of peaks between the electrical resistance curve and the cyclic strain curve could be attributed to the high viscoelasticity of the Ecoflex substrate, which can be remedied by using other stretchable substrates with low viscoelasticity such as PDMS or by reducing the strain loading rate (Figure S5, Supporting Information). To evaluate the response time of the CSF strain sensor, a quasi-transient step strain of 0.5% was loaded and the responsive time was determined to be less than 70 ms according to the high-resolution resistance–time curve (Figure S6; see Supporting Information for details). Figure 3e shows the hysteresis of resistance during loading-unloading

Adv. Mater. **2016**,
DOI: 10.1002/adma.201601572

cycles under different applied strain, which could also be attributed to the viscoelasticity of the Ecoflex. Besides, the CSF strain sensor showed overshoots with a short creep recovery time of 2, 6, and 9 s when being stretched up to 100%, 200%, and 300% at a strain rate of 40% s^{-1}, manifesting the low creep of the strain sensor (Figure 3f). After the recovery of the overshoot, the resistance of the CSF strain sensor remained stable, indicating its reliable performance. Stability and durability are of great importance for practical applications of strain sensors. As shown in Figure 3g, the electrical response of the CSF strain sensor exhibited high stability during 6000 loading and unloading cycles of 100% strain except for overshoot of the incipient cycles which also arises from the Ecoflex. The CSF strain sensor further displayed stable properties even after being subjected to 10 000 cycles of 300% strain (Figure S7, Supporting Information). From the above, one can see that the CSF strain sensor showed merit of ultrastretchability, high sensitivity, fast response, low creep. and excellent durability concurrently (see Table S2 (Supporting Information) for a detailed comparison of the main performance of the CSF strain sensor and the other reported typical carbon-based strain sensors).

To understand the working mechanism of the CSF strain sensors, we tracked the structure evolution of a sensor during the first loading (**Figure 4**a) and subsequent loading (Figure 4b) of strain in *y*-direction. As shown in Figure 4a, the first time stretching led to irreversible cracks throughout the structure, resulting in the formation of islands and gaps. The number of islands and gaps as well as the width of the gaps increased with the augment of strain, contributing to the monotonically increase of the resistance (Figure S8, Supporting Information). Importantly, the islands kept the integrity of the woven structure (Figure 4c) and the gaps were bridged by the parallel fibers of yarns in the *x*-direction (Figure 4d), which prevented rupturing of the conductive pathways under extremely large deformation and was vital to the extraordinary stretchability. The fracture of the twisted yarns in the y direction allows for the high sensitivity. As shown in Figure 4b, during the subsequent loading, the gap widths enlarged as the applied strain

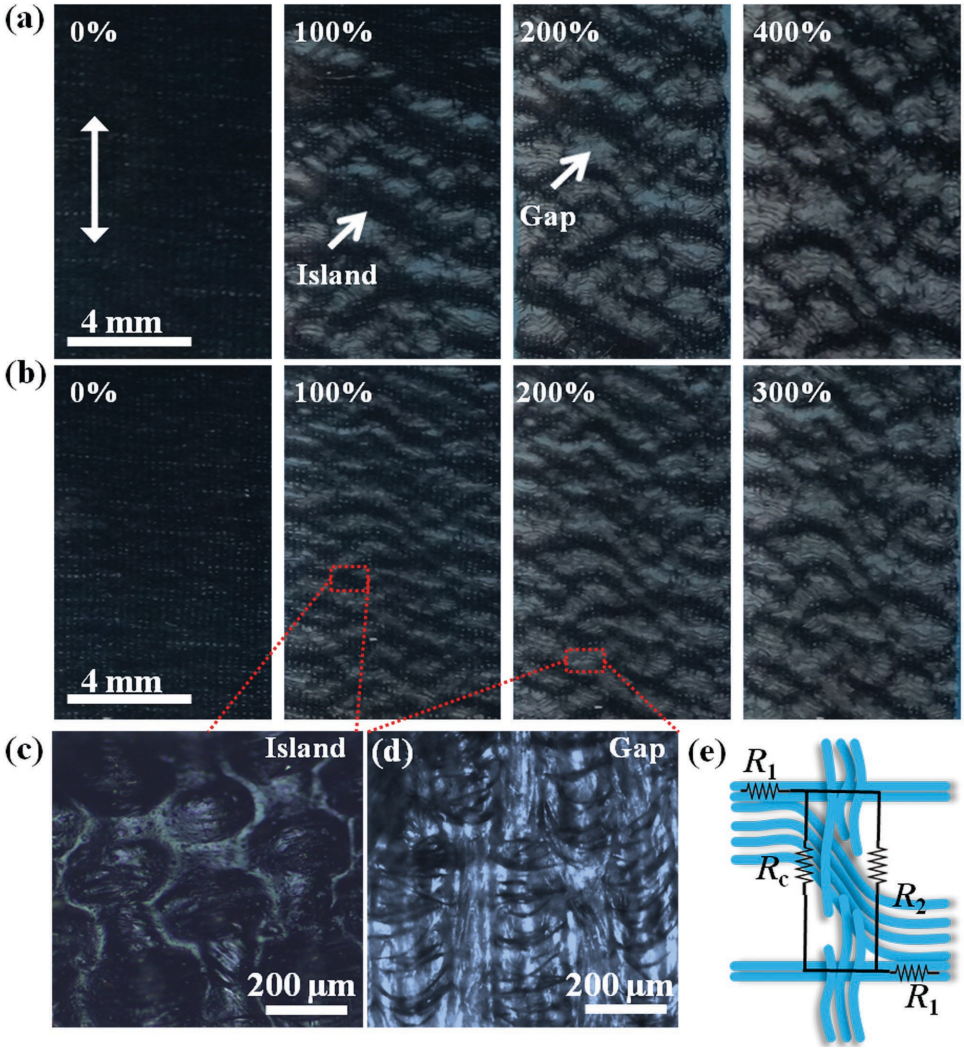

Figure 4. Working mechanism of the plain-weave CSF strain sensor. Photographs of a CSF strain sensor during (a) initial loading of 400% strain and (b) subsequent loading of 300% strain. Optical images of (c) the island and (d) gap formed under tensile strain. e) Schematic illustration showing the resistance model of an elementary unit.

increased with no new gaps and islands arising, which was crucial for the remarkable durability. The unique plain-weave structure of CSF, where there are parallel fibers in one direction and twisted fibers in another direction (the direction being stretched), is critical for the outstanding performance of the CSF strain sensors.

To confirm the role of the parallel fibers for the exceptional stretchability of the CSF strain sensor, we removed some of the yarns in x direction from a piece of plain-weave silk fabric and fabricated another strain sensor. As expected, the obtained sensor showed a smaller tolerant strain but a higher GF (Figure S9a, Supporting Information), proving the vital role of the parallel fibers for the excellent stretchability and also providing a simple solution to fabricate strain sensors with higher sensitivity but less stretchability. Different initial fabrics could be utilized for the fabrication of strain sensors for different purpose. Besides, we found that the CSF strain sensors, whether made from plain-weave, twill-weave or satin-weave silk fabrics, all exhibited larger workable strain range when being stretched in y direction than in the *x*-direction (Figure S9b–d, Supporting Information), which further confirmed that parallel fibers perpendicular to the tensile direction contributed to the extraordinarily stretchability. When the plain-weave CSF strain sensor was stretched in x direction, islands and gaps formed while the gaps were not bridged by fibers because of the twisted configuration of yarns in y direction (Figure S10a, Supporting Information), which accounted for its small workable strain range. Compared to plain-weave structures, CSF strain sensors based on twill- and satin- weave fabric showed less islands and wide gaps under tensile strain (Figure S10b–e, Supporting Information), which could be understood considering the fact that twill- and satin- weave structures possess less interlacing points between warp/weft yarns than the plain-weave structure. The difference in morphology evolution under strain explains the smaller tolerable strain range of the twill- and satin- weave CSF strain sensors than that of the plain-weave CSF strain sensors. Besides, the interlock-stitch fabric based strain sensors showed gaps with no bridging fibers no matter being stretched in which direction (Figure S10f,g, Supporting Information), interpreting their much lower tolerable strain.

To understand our observation that the resistance of the CSF strain sensor increased with strain monotonically but with two consecutive linear regions of different GF, we developed a simple model, as shown in Figure 4e. The resistance of the fractured CSF, which is composed of islands, fractured warp yarns and partially suspended fibers from the weft yarns, could be calculated with Equation (1)

$$R = \frac{2R_1R_2 + 2R_1R_c + R_2R_c}{R_2 + R_c} \quad (1)$$

where R_1, R_2, and R_c are the resistances of the island, the bridged fibers from the weft yarn and the contact resistance between fractured warp yarn and weft yarn, respectively. During the stretch, it is assumed the resistance of the island (R_1) is constant while R_2 (bridge extension) and R_c (contact area increase) increase linearly with tensile strain. Equation (1) can describe the resistance for the whole strain range. However, for large strain region (250–500% strain for the plain-weave CSF strain sensors), the fractured warp yarns cannot contact with the weft yarns, resulting in that the contact resistance (R_c) becomes infinite, and the equation becomes $R = 2R_1 + R_2$. The above model and analysis explicitly interpret the existence of two linear regions in Figure 3b. More analysis could be seen in the Supporting Information discussion and Figure S11.

Owing to the excellent flexibility, high sensitivity and broad working range, CSF strain sensors possess tremendous potential applications in wearable devices for full-range recognition of human activities. We demonstrated the applications of CSF strain sensors for detection of both large motions and subtle motions. **Figure 5**a–e shows the ability of CSF strain sensors in detection of vigorous human motions, such as motion of joints. To facilitate the detection of large human motions, the strain sensors could be assembled on clothes or accessories. Figure 5a shows a glove assembled with five individual CSF strain sensors, which can monitor real-time motions of fingers. As shown in Figure 5b, bending of the fingers could be precisely tracked by monitoring the relative change of the resistance. Figure 5c shows a wrist guard integrated with a CSF strain sensor, which can distinguish and monitor the bending and rotating of a wrist (Figure 5d). The CSF strain sensor could also be integrated on stocking/tights (Figure 5e) to detect and discriminate the motions of knee joints, such as extending/flexing, marching, jogging, jumping and combination of squatting and jumping (Figure 5f). Besides, the motions of elbows and ankle joints could also be similiarly recorded and distinguished by the wearable CSF sensors, based on the apparently differentiable patterns of response curves (Figure S12a–d, Supporting Information). In addition to monitoring large motions of human, the CSF strain sensor could also be applied in robotics to realize real-time detection of joint movements of robotics, as demonstrated in Figure S12e (Supporting Information).

Subtle human motions, such as pulse, respiration, tiny muscle movement, and phonation, could also be promptly and accurately detected by the CSF strain sensor. For demonstration, we attached CSF strain sensors at the corner of a eye (insets in Figure 5g) and the cheek (insets in Figure S11f,g, Supporting Information) of a human face to monitor the subtle muscle movements induced by microexpression. The resistance change of the sensors, corresponding to the stretching of facial muscle, induced by blinking (Figure 5g), facial expression changing from a poker face to a smile face (Figure S11f, Supporting Information), and cheek bulging (Figure S11g, Supporting Information), could be precisely recorded. Besides, pulse is a very important physiological signal for the systolic and diastolic blood pressure as well as the heart rate. Figure 5h shows a CSF sensor attached to a wrist band, which is placed over the radial artery to detect the pulse. Figure 5i presents the real-time resistance change signal of the sensor under relaxation and exercise conditions. It clearly displays repeatable and regular pulse shapes in relaxation with frequency of 70 beats min^{-1}, in contrast to the irregular shapes after exercise with frequency of 110 beats min^{-1}. The close-up of a single pulse peak in relaxation clearly reveals typical characteristics of the pulse waveform, namely, the percussion wave (*P*-wave), tidal wave (*T*-wave) and diastolic wave (*D*-wave),[48] demonstrating the high sensentivity of the CSF strain sensor. The wearable CSF sensor was assembled on a tight to monitor respiration, which is also

Adv. Mater. **2016**,
DOI: 10.1002/adma.201601572

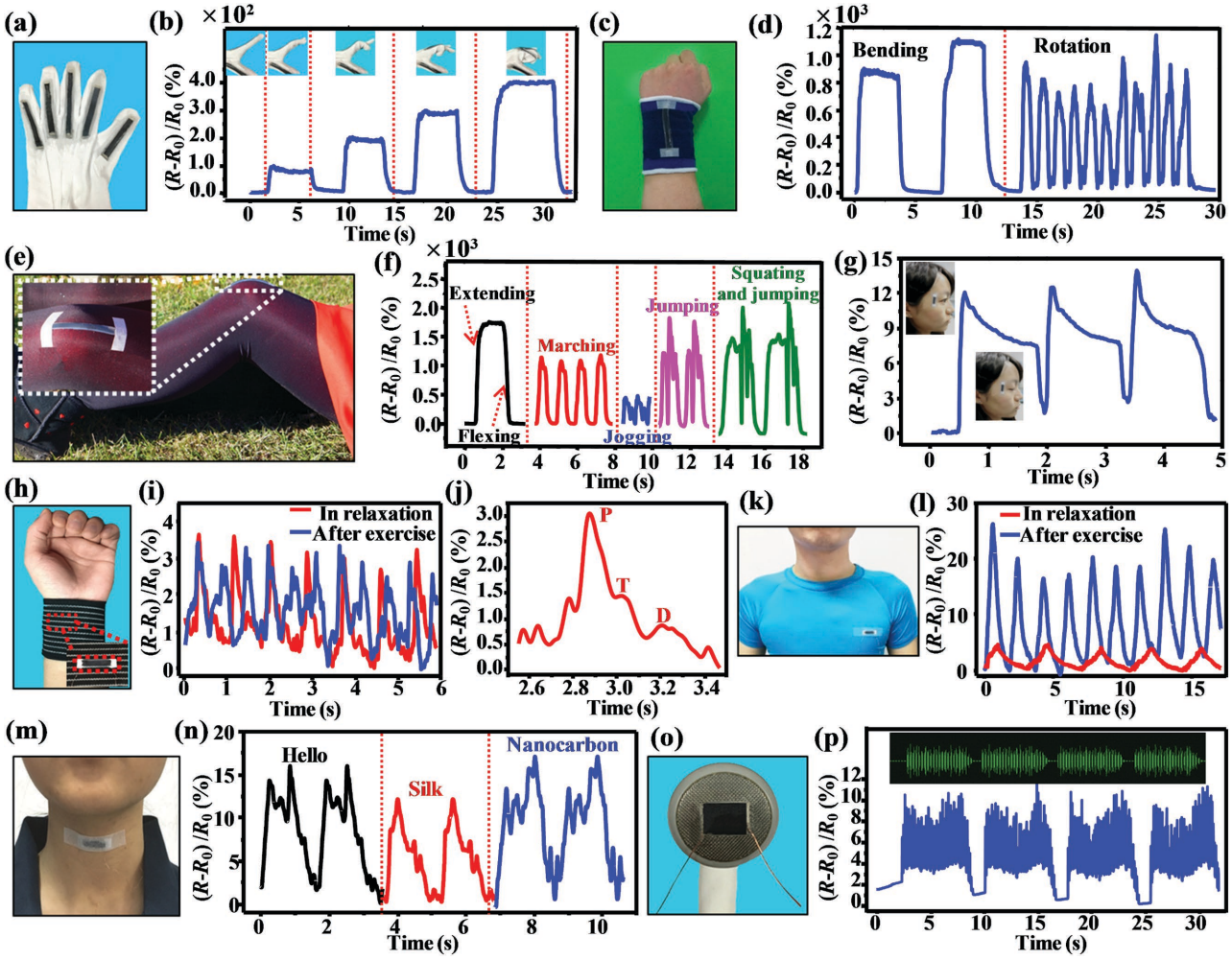

Figure 5. Detection of various human motions and sounds using the wearable CSF strain sensors. Photographs of the wearable sensors assembled on (a) a glove, (c) a wrist guard, and (e) a stocking, and the corresponding signals of the (b) bending of fingers, (d) bending and rotation of a wrist, and (f) flexing/extending, marching, jogging, jumping, and squatting-jumping of a knee joint. g) Signals showing the tiny muscle movement caused by blinking. Insets: photographs of eye-opening and eye-closing. Photographs of the sensors attached to (h) a wrist band, (k) a tight, (m) throat, and (i,j) the corresponding signals of pulse, (l) inspiration, (n) phonation when the wearer spoke "Hello," "Silk," and "Nanocarbon." o) Photograph showing a sensor attached on an earphone. p) Signals of the sensor corresponding to a warble audio. Inset: the sound wave profile.

an important physiological signal (Figure 5k). Figure 5l shows the resistance change of the sensor in relaxation and after exercise, which explicitly manifests the discriminable respiration rate and depth determined by the amplitude of the peaks, indicating the potential applications of the wearable sensors for monitoring apnea in adults and sudden infant death syndrome. In addition, the CSF strain sensor could also be attached onto the throat to monitor the tiny epidermis and muscle movement during speech to recognize phonation (Figure 5m). As shown in Figure 5n, the sensor displayed distinguishable and repeatable signal patterns when the wearer spoke different words. The fast and sensitive recognition of phonation endows the CSF strain sensor potential applications in human/machine interaction and phonation rehabilitation training.

Besides, sound signals could also be recognized by the CSF strain sensor. An earphone with a CSF strain sensor attached on its vibrating membrane (Figure 5o) was used to play different audio files (Audio S1–S3, Supporting Information) and the sensor generated the corresponding resistance change signals. As shown in Figure 5p, the sensor showed an almost synchronous response to the sound wave profile of the warble audio (inset in Figure 5p) and most of the characteristic peaks were retained. The performance for respond to other audios, such as phone beeps audio and moo audio, is also excellent (Figure S12h,i, Supporting Information).

Furthermore, the CSF strain sensors could be used for reconstruction of human motions with the assistance of a computer program. As a proof of concept, the wearable strain sensors were assembled onto the elbow and shoulder joints to monitor the motions of upper limbs (Figure S13a–h, Supporting Information). The signals induced by the motions were received and transformed by a motion reconstruction program and the corresponding motions could be displayed in real time on a computer (Figure S13i–p, Supporting Information) (see details in the Experimental Section). A movie which visually exhibits the concept could be found in the Supporting Information (Movie S1).

Based on the above results and the extremely wide sensing range and remarkable sensitivity of the wearable strain sensors, we believe the possibility of rebuilding the movements of all the human motions.

In summary, we fabricated wearable strain sensors with combined high sensitivity and high stretchability through a simple carbonization process, based on the unique chemical components as well as the woven structures of silk fabric. The CSF strain sensors derived from plain-weave silk fabric showed a tolerable strain of more than 500%, and GF of 9.6 (for strain within 250%) and 37.5 (for strain of 250–500%). Furthermore, the CSF sensors had fast response (<70 ms) and high durability (>10 000 cycles). As proved by both of experimental observations and theoretical analysis, the unique hierarchical structures of the plain-weave silk fabric contribute to the superior properties of the strain sensors. We demonstrated that the CSF strain sensors could be used for monitoring both of vigorous human motions, such as jumping, marching, jogging, bending, and rotation of joints, and subtle motions, such as facial expression, pulse, respiration, and phonation, indicating their tremendous potential applications in wearable electronics and intelligent robots. To the best of our knowledge, it is the first time to utilize carbonized fabrics as sensing elements, which takes the advantage of the chemical structures as well as the unique woven structures of mass-produced fabrics. The concept could be readily extended to other fabrics, such as cotton, modal, wool fabrics, and other artificial or natural fiber fabrics, paving a new way for the low-cost and large-scale fabrication of wearable strain sensors.

Experimental Section

Fabrication of CSF Strain Sensors: Commercial available silk fabrics with plain-weave, twill-weave, satin-weave and interlock-stitch structures were utilized as raw materials. The fabrics were carbonized under an argon (purity, 99.999%; gas flow, 100 sccm) and hydrogen (purity, 99.999%; gas flow, 10 sccm) mixed atmosphere in a tube furnace with the following heat treatment schedule: i) heat from 25 to 150 °C at a rate of 10 °C min^{-1} and keep for 60 min; ii) then heat to 350 °C at a rate of 5 °C min^{-1} and keep for 180 min; iii) heat to 950 °C at a rate of 3 °C min^{-1} and keep for 120 min; iv) naturally cool the system to room temperature. The obtained CSF were cut into rectangular strips and then were connected to copper wires at both of the two ends with silver paste. Afterward, the CSF strip was put on a Ecoflex substrate (a 1:1 mixture of Ecoflex part A and part B, Ecoflex Supersoft 0050, smooth-on, Inc.) and then liquid Ecoflex was dropped on the surface to fix and encapsulate the device. Finally, the samples were cured at room temperature for 12 h. The thickness of the Ecoflex in the final samples was around 550 μm.

Characterization of Structures and Performance of the Sensors: The morphologies and structures of materials were characterized by a field emission SEM (FE-SEM, FEI Quanta 650) and a field emission TEM (FE-TEM, JEOL JEM2010F). Raman spectra were performed with a Raman spectroscope (HORIBA HR800) with a laser excitation wavelength of 532 nm. XPS analysis was performed using Al K_α radiation (Thermo Scientific Escalab 250Xi). The morphology evolution of the CSF strain sensor with applied strain was characterized by a camera and an optical microscope (LEICA DM2500 M). The loading of tensile strain was performed with a universal testing machine (SHIMADZU AGS-X), while the electrical signals of the strain sensors were recorded at the same time by a Keithley 2400 digital meter at a constant voltage of 3 V.

Reconstruction of Human Body Motions: To reconstruct the human body motions, the CSF strain sensors were attached onto different joints of the human body, such as elbows and shoulders, using commercial medical adhesive tapes. The self-designed system for the motion reconstruction includes two main parts, namely, the wireless motion capture module and the motion reconstruction module (see details in Supporting Information, Figure S14).

Supporting Information

Supporting Information is available from the Wiley Online Library or from the author.

Acknowledgements

This work was supported by the NSF of China (51422204, 51372132),the National Key Basic Research and Development Program (No. 2013CB228506), and the Cyrus Tang Foundation(202003).

Received: March 22, 2016
Published online:

[1] A. A. Argun, A. Cirpan, J. R. Reynolds, *Adv. Mater.* **2003**, *15*, 1338.
[2] J. A. Rogers, T. Someya, Y. Huang, *Science* **2010**, *327*, 1603.
[3] D. J. Lipomi, B. C. K. Tee, M. Vosgueritchian, Z. Bao, *Adv. Mater.* **2011**, *23*, 1771.
[4] Y. Kim, J. Zhu, B. Yeom, M. Di Prima, X. Su, J.-G. Kim, S. J. Yoo, C. Uher, N. A. Kotov, *Nature* **2013**, *500*, 59.
[5] J. Lee, P. Lee, H. B. Lee, S. Hong, I. Lee, J. Yeo, S. S. Lee, T. S. Kim, D. Lee, S. H. Ko, *Adv. Funct. Mater.* **2013**, *23*, 4171.
[6] T. Q. Trung, S. Ramasundaram, B. U. Hwang, N. E. Lee, *Adv. Mater.* **2016**, *28*, 502.
[7] J. H. Ahn, J. H. Je, *J. Phys. D: Appl. Phys.* **2012**, *45*, 103001.
[8] J. R. Windmiller, J. Wang, *Electroanalysis* **2013**, *25*, 29.
[9] J. Park, I. You, S. Shin, U. Jeong, *ChemPhysChem* **2015**, *16*, 1155.
[10] W. T. Park, J. R. MallonJr, A. J. Rastegar, B. L. Pruitt, *Proc. IEEE* **2009**, *97*, 513.
[11] A. Ajovalasit, B. Zuccarello, *J. Strain Anal. Eng. Des.* **2005**, *40*, 643.
[12] J. Kim, M. Lee, H. J. Shim, R. Ghaffari, H. R. Cho, D. Son, Y. H. Jung, M. Soh, C. Choi, S. Jung, *Nat. Commun.* **2014**, *5*, 5747.
[13] D. Kang, P. V. Pikhitsa, Y. W. Choi, C. Lee, S. S. Shin, L. Piao, B. Park, K.-Y. Suh, T. i. Kim, M. Choi, *Nature* **2014**, *516*, 222.
[14] B. U. Hwang, J. H. Lee, T. Q. Trung, E. Roh, D. I. Kim, S. W. Kim, N. E. Lee, *ACS Nano* **2015**, *9*, 8801.
[15] Y. Y. Zhang, C. J. Sheehan, J. Y. Zhai, G. F. Zou, H. M. Luo, J. Xiong, Y. T. Zhu, Q. X. Jia, *Adv. Mater.* **2010**, *22*, 3027.
[16] T. Yamada, Y. Hayamizu, Y. Yamamoto, Y. Yomogida, A. Izadi-Najafabadi, D. N. Futaba, K. Hata, *Nat. Nanotechnol.* **2011**, *6*, 296.
[17] L. Cai, L. Song, P. Luan, Q. Zhang, N. Zhang, Q. Gao, D. Zhao, X. Zhang, M. Tu, F. Yang, *Sci. Rep.* **2013**, *3*, 3048.
[18] J. Park, Y. Lee, J. Hong, Y. Lee, M. Ha, Y. Jung, H. Lim, S. Y. Kim, H. Ko, *ACS Nano* **2014**, *8*, 12020.
[19] S. Ryu, P. Lee, J. B. Chou, R. Xu, R. Zhao, A. J. Hart, S. G. Kim, *ACS Nano* **2015**, *9*, 5929.
[20] Z. Liu, D. Qi, P. Guo, Y. Liu, B. Zhu, H. Yang, Y. Liu, B. Li, C. Zhang, J. Yu, *Adv. Mater.* **2015**, *27*, 6230.
[21] Y. Wang, R. Yang, Z. Shi, L. Zhang, D. Shi, E. Wang, G. Zhang, *ACS Nano* **2011**, *5*, 3645.
[22] M. Hempel, D. Nezich, J. Kong, M. Hofmann, *Nano Lett.* **2012**, *12*, 5714.
[23] C. S. Boland, U. Khan, C. Backes, A. O'Neill, J. McCauley, S. Duane, R. Shanker, Y. Liu, I. Jurewicz, A. B. Dalton, *ACS Nano* **2014**, *8*, 8819.

DOI: 10.1002/adma.201601572

[24] C. Yan, J. Wang, W. Kang, M. Cui, X. Wang, C. Y. Foo, K. J. Chee, P. S. Lee, *Adv. Mater.* **2014**, *26*, 2022.
[25] Y. Cheng, R. Wang, J. Sun, L. Gao, *Adv. Mater.* **2015**, *27*, 7365.
[26] J. Zhao, G. Wang, R. Yang, X. Lu, M. Cheng, C. He, G. Xie, J. Meng, D. Shi, G. Zhang, *ACS Nano* **2015**, *9*, 1622.
[27] J. J. Park, W. J. Hyun, S. C. Mun, Y. T. Park, O. O. Park, *ACS Appl. Mater. Interfaces* **2015**, *7*, 6317.
[28] N. Lu, C. Lu, S. Yang, J. Rogers, *Adv. Funct. Mater.* **2012**, *22*, 4044.
[29] S. Lim, D. Son, J. Kim, Y. B. Lee, J. K. Song, S. Choi, D. J. Lee, J. H. Kim, M. Lee, T. Hyeon, *Adv. Funct. Mater.* **2015**, *25*, 375.
[30] M. K. Choi, I. Park, D. C. Kim, E. Joh, O. K. Park, J. Kim, M. Kim, C. Choi, J. Yang, K. W. Cho, *Adv. Funct. Mater.* **2015**, *25*, 7109.
[31] S. Jung, J. H. Kim, J. Kim, S. Choi, J. Lee, I. Park, T. Hyeon, D. H. Kim, *Adv. Mater.* **2014**, *26*, 4825.
[32] M. A. Yahya, Z. Al-Qodah, C. Z. Ngah, *Renewable Sustainable Energy Rev.* **2015**, *46*, 218.
[33] L. D. Koh, Y. Cheng, C. P. Teng, Y. W. Khin, X. J. Loh, S. Y. Tee, M. Low, E. Ye, H. D. Yu, Y. W. Zhang, *Prog. Polym. Sci.* **2015**, *46*, 86.
[34] A. T. Nguyen, Q. L. Huang, Z. Yang, N. Lin, G. Xu, X. Y. Liu, *Small* **2015**, *11*, 1039.
[35] S. Y. Cho, Y. S. Yun, S. Lee, D. Jang, K. Y. Park, J. K. Kim, B. H. Kim, K. Kang, D. L. Kaplan, H. J. Jin, *Nat. Commun.* **2015**, *6*, 7145.
[36] J. Hou, C. Cao, F. Idrees, X. Ma, *ACS Nano* **2015**, *9*, 2556.
[37] Y. S. Yun, S. Y. Cho, J. Shim, B. H. Kim, S. J. Chang, S. J. Baek, Y. S. Huh, Y. Tak, Y. W. Park, S. Park, *Adv. Mater.* **2013**, *25*, 1993.
[38] Y. Wang, Y. Song, Y. Wang, X. Chen, Y. Xia, Z. Shao, *J. Mater. Chem. A* **2015**, *3*, 773.
[39] Y. J. Kim, Y. Abe, T. Yanagiura, K. C. Park, M. Shimizu, T. Iwazaki, S. Nakagawa, M. Endo, M. S. Dresselhaus, *Carbon* **2007**, *45*, 2116.
[40] Y. S. Yun, K. Y. Park, B. Lee, S. Y. Cho, Y. U. Park, S. J. Hong, B. H. Kim, H. Gwon, H. Kim, S. Lee, *Adv. Mater.* **2015**, *27*, 6914.
[41] J. Zhang, Y. Cai, Q. Zhong, D. Lai, J. Yao, *Nanoscale* **2015**, *7*, 17791.
[42] B. Zhu, H. Wang, W. R. Leow, Y. Cai, X. J. Loh, M. Y. Han, X. Chen, *Adv. Mater.* **2015**, DOI: 10.1002/adma.201504276.
[43] T. Hu, D. L. Kaplan, F. G. Omenetto, *Adv. Mater.* **2012**, *24*, 2824.
[44] S. B. Yoon, G. S. Chai, S. K. Kang, J. S. Yu, K. P. Gierszal, M. Jaroniec, *J. Am. Chem. Soc.* **2005**, *127*, 4188.
[45] M. E. Rousseau, T. Lefevre, L. Beaulieu, T. Asakura, M. Pézolet, *Biomacromolecules* **2004**, *5*, 2247.
[46] S. H. Lim, R. Li, W. Ji, J. Lin, *Phys. Rev. B* **2007**, *76*, 195406.
[47] C. Farcau, N. M. Sangeetha, H. Moreira, B. T. Viallet, J. Grisolia, D. Ciuculescu-Pradines, L. Ressier, *ACS Nano* **2011**, *5*, 7137.
[48] X. Wang, Y. Gu, Z. Xiong, Z. Cui, T. Zhang, *Adv. Mater.* **2014**, *26*, 1336.

ADVANCED MATERIALS

Supporting Information

for *Adv. Mater.*, DOI: 10.1002/adma.201601572

Carbonized Silk Fabric for Ultrastretchable, Highly Sensitive, and Wearable Strain Sensors

*Chunya Wang, Xiang Li, Enlai Gao, Muqiang Jian, Kailun Xia, Qi Wang, Zhiping Xu, Tianling Ren, and Yingying Zhang**

Submitted to ADVANCED MATERIALS

Supporting Information

Carbonized Silk Fabric for Ultra-stretchable, Highly Sensitive and Wearable Strain Sensors

Chunya Wang, Xiang Li, Enlai Gao, Muqiang Jian, Kailun Xia, Qi Wang, Zhiping Xu, Tianling Ren and Yingying Zhang*

This supporting file includes:

- Supporting Figure S1 to S14
- Supporting Table S1 and Table S2
- Supporting Discussions related to Figure S3, Figure S6, Figure S11 and Figure S14

The sequence is the same as they are mentioned in the main text.

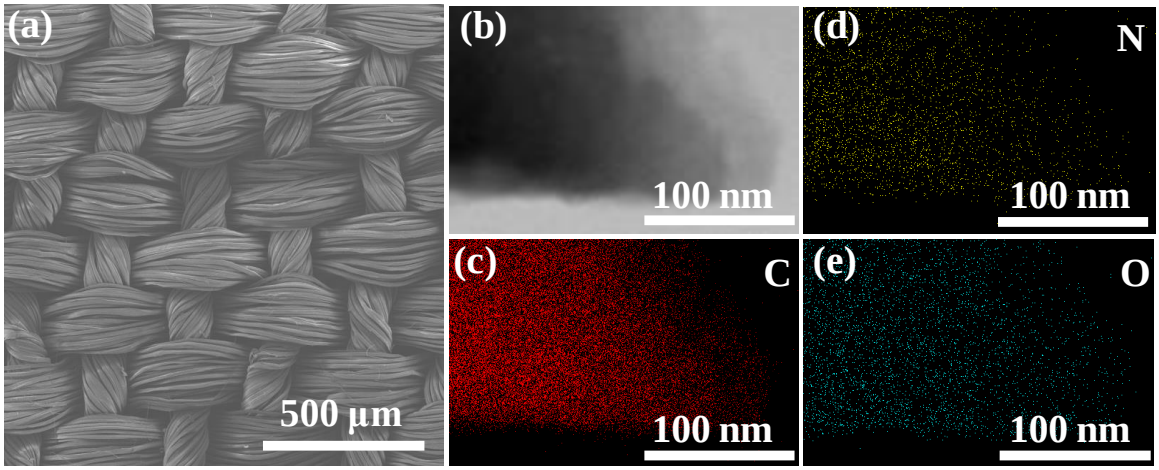

Figure S1. (a) SEM image of a pristine plain-weave silk fabric. (b-e) TEM image (b) and corresponding EDX mappings of C (c), N (d) and O (e) elements.

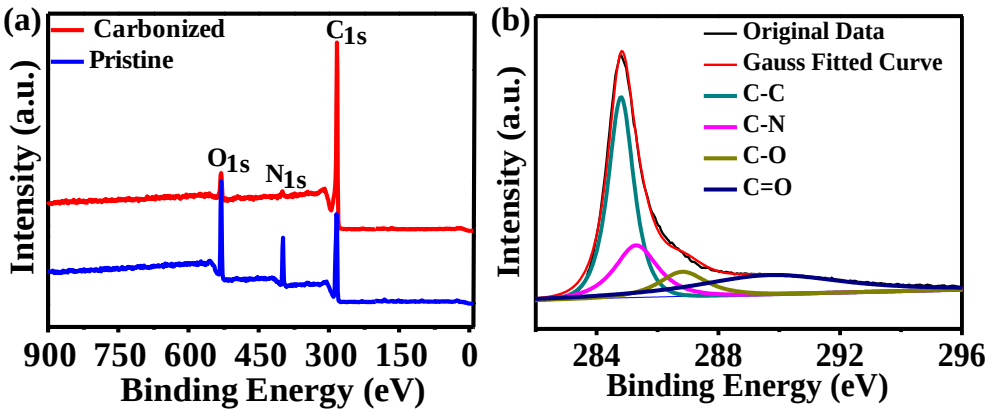

Figure S2. (a) XPS survey spectrum of the pristine and carbonized silk fabric and (b) high-resolution spectrum of C1s XPS peak of the carbonized silk fabric.

Table S1. Atomic composition of pristine and carbonized silk fabric.

	Atomic Composition (%)	
	Pristine silk fabric	**Carbonized silk fabric**
C	62.6	91.2
N	17.0	2.7
O	20.4	6.1

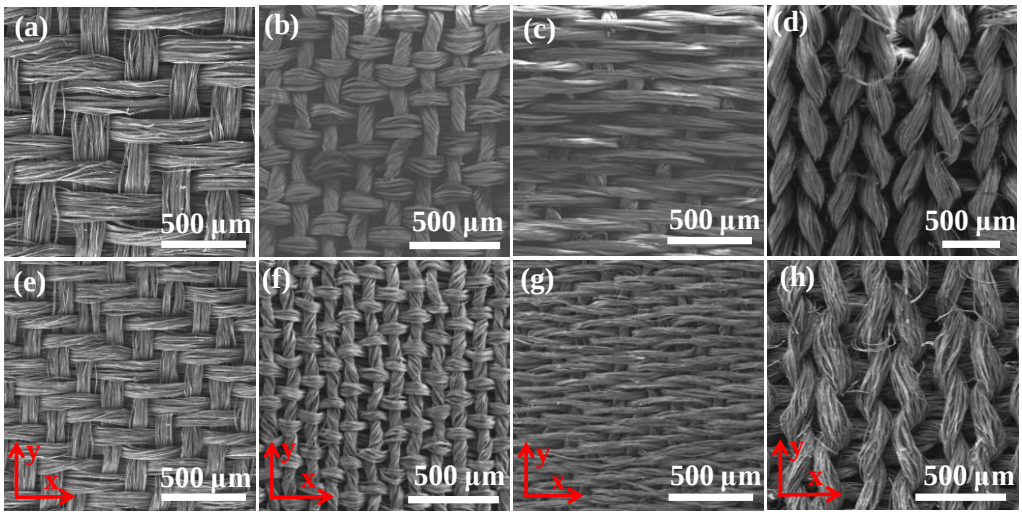

Figure S3. SEM images of pristine silk fabrics with twill-weave (a), two sides of satin-weave (b, c) and interlock-stitch (d) and corresponding carbonized fabric with twill-weave (e), satin-weave (f, g) and interlock-stitch (h).

Figure S3 show the morphologies of pristine and carbonized silk fabrics with twill-weave, satin-weave and interlock-stitch structures. It is obvious that the yarns in both x and y direction of twill-weave silk fabric are composed of parallel fibers, and the yarn density in x direction is larger than that in y direction. The yarns in x direction and y direction of satin-weave silk fabric consist of parallel fibers and twisted fibers, respectively.

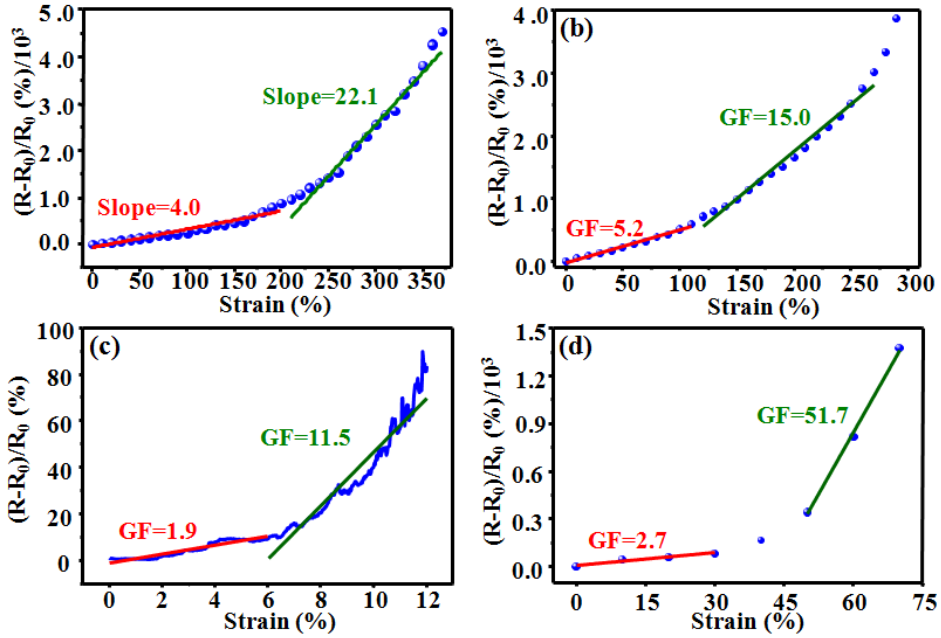

Figure S4. Relative change in resistance of the CSF strain sensors being stretched in y direction with twill weave structure (a) and satin weave structure (b). Relative change in resistance of carbonized silk fabric based strain sensor with interlock stitch structure being stretched in y direction (c) and x direction (d).

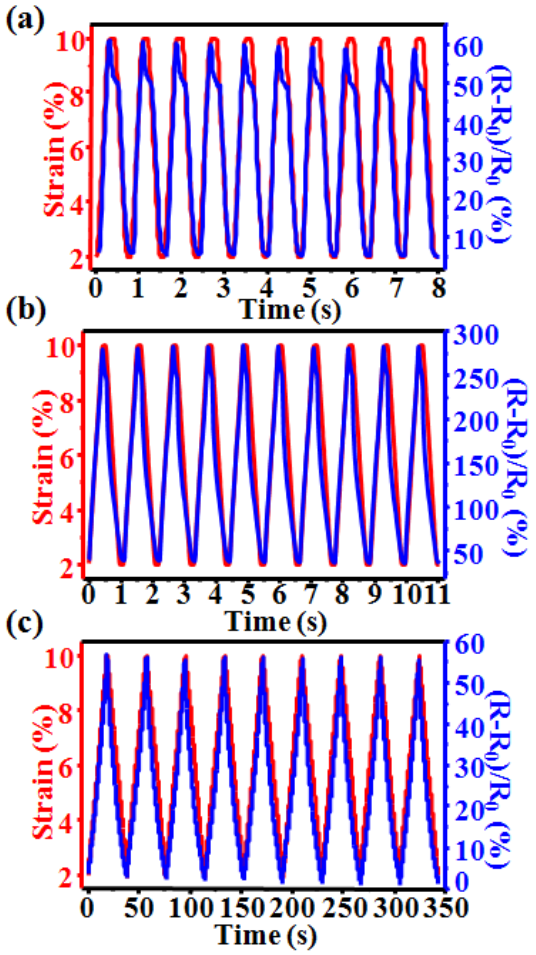

Figure S5. Relative change in resistance (blue) for cycling between 2%-10% strain (red) at 1.25 Hz with Ecoflex as substrate (a), at 1 Hz with PDMS as substrate (b) and at 0.026 Hz with Ecoflex as substrate (c).

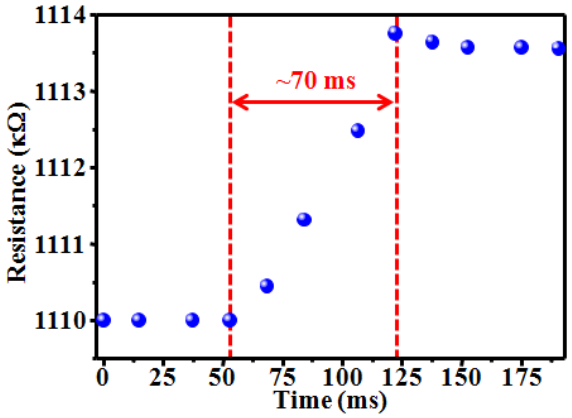

Figure S6. The real-time resistance of the CSF strain sensor subjected to a quasi-transient step strain of 0.5%, showing a response time of around 70 ms.

Determination of the response time of the CSF strain sensor:

To determine the response time, a quasi-transient step strain of 0.5% was applied on the CSF based strain sensor. As the sample length was 12 mm, the maximum stretching speed of the used universal testing machine was 900 mm/min, thus the time duration for the step-strain was 4 ms, which could be considered as a quasi-transient process. The real-time resistance change of the strain senor versus time was shown in Figure S6, from which it is obvious that the resistance change was completed in about 70 ms, indicating that the response time should be less than 70 ms.

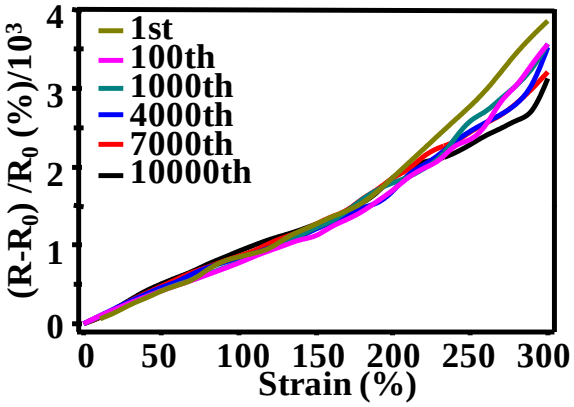

Figure S7. Relative change in resistance for multiple-cycle tests with strain from 0%-300%.

Table S2. Comparison of main performance of the CSF strain sensor and recently reported carbon-based strain sensors with large sensing range.

Strain sensors	*Maximal workable strain range*	*Average gauge factor*	*Durability*	*Response time*	*Creep recovery time*	*Working voltage*
Our work: carbonized plain-weave silk fabric with Ecoflex encapsulated	**500%**	**5.8 (under 1% strain); 9.6 (within 250% strain); 37.5 (250%-500% strain)**	**10,000cycles at 300% strain**	**70 ms**	**2 s (100% strain); 6 s (200% strain) ; 9 s (300% strain)**	**3 V**
Graphene based fiber with "compression spring" Structure [1]	100%	10 (1% Strain), 3.7 (50% Strain)	10,000 cycles at 50% strain	100 ms	2 s (10% strain)	5 V
Graphene Rubber Composite [2]	800%	35	1,000 cycles at ~100% strain	Not shown	Not shown	Not shown
Graphene–Nanocellulose Nanopaper [3]	100%	1.6 (10% strain）, 7.1 (100% strain)	Not shown	Not shown	Not shown	Not shown
Carbon nanotube fiber on pre-strain Ecoflex [4]	960%	0.56 (200% strain); 47 (200%-400% strain); 64 (400-960% strain)	10,000 cycles at ~300% strain	10 ms	12 ms	Not shown
Carbon nanotube film on PDMS [5]	280%	0.82 (40% strain); 0.06 (60-200% strain)	10,000 cycles at 200% strain	14 ms	5 s	Not shown
Carbon black thermal plastic elastomer composite [6]	80%	20	3,600 cycles At ~80% strain	Not shown	Not shown	Not shown

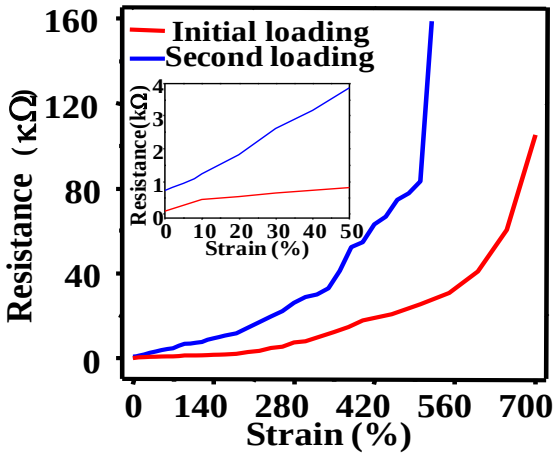

Figure S8. The resistance of a CSF strain sensor for the initial loading (red) and second loading (blue).

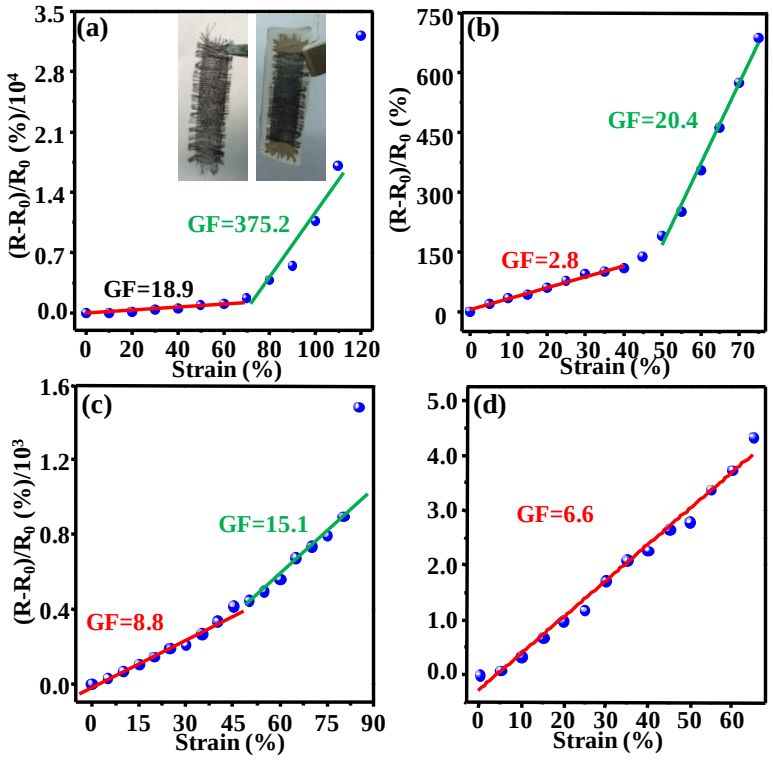

Figure S9. (a) Relative change in resistance of a carbonized loose plain-weave silk fabric based strain sensor being stretched in y direction. (b-d) Relative change in resistance of CSF strain sensor being stretched in x direction with plain-weave (b), twill-weave (c) and satin-weave structure (d).

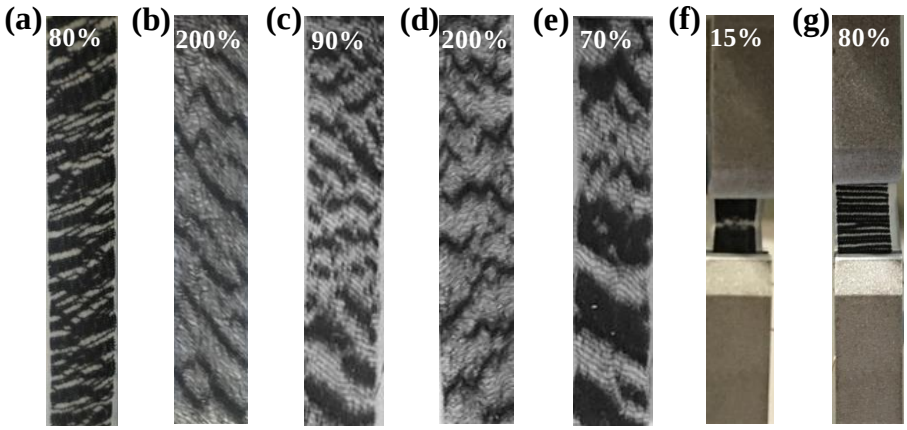

Figure S10. The morphology of carbonized silk fabric based strain sensors with plain-weave being stretched in x direction (a), twill-weave being stretched in y direction (b) and x direction (c), satin-weave being stretched in y direction (d) and x direction (e), interlock-stitch being stretched in y direction (f) and x direction (g).

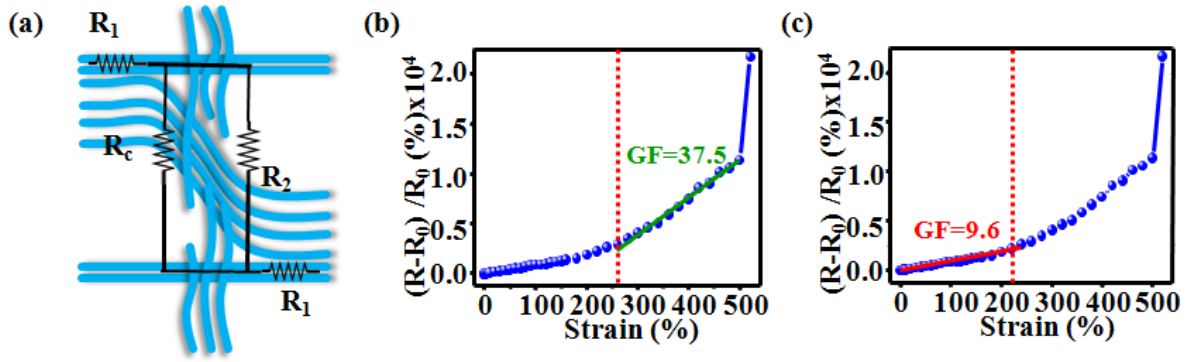

Figure S11. Resistance model. (a) Schematic illustration of the modeling structure. R_1 and R_2 represent the resistance of the island and the suspended fibers from weft yarns, R_c refers to the contact resistance between fractured warp yarns and weft yarns. (b) Linear relationship between relative resistance change and large scale strain (250%-500% strain), which can be used to determine R_c. (c) Linear relationship between relative resistance change and small scale strain (within 250% strain), which can be used to determine R_2.

Figure S11a illustrate the resistance model of the fractured carbonized silk fabric which is composed of the islands, the fractured warp yarns and the suspended fibers from the weft yarns. According to this model, the resistance (R) could be decrisbed as follows:

$$R=\frac{2R_1R_2+2R_1R_c+R_2R_c}{R_2+R_c} \quad (1)$$

where R_1, R_2 and R_c are respectively the resistances of the island, the bridged fibers from the weft yarn and the contact resistance between fractured warp yarn and weft yarn. During the stretch, the resistance (R_1) of the island could be reasonably assumed as constant; R_2 (bridge extension) and R_c (contact area increase) could be assumed to increase linearly with strain (ε), namely, R_2 and R_c can be described as $R_2=X\times\varepsilon$ and $R_c=Y\times\varepsilon$, respectively. Obviously, the initial resistance of the elementary unit (R_0) with no strain applied is equal to $2R_1$. Therefore, the relative resistance change can be described as:

$$\frac{R-R_0}{R_0}=\frac{X\times Y\times\varepsilon}{2(X+Y)*R_1} \quad (2)$$

From the resistance curve of the CSF strain sensor (Figure S8), R_1 could be determined to be 0.36 kΩ. For large strain region (250%-500% strain for the plain-weave CSF strain sensor), the fractured warp yarns could not contact with the weft yarns, resulting in that the contact resistance R_c becomes infinite, the relative resistance change becomes:

$$\frac{R-R_0}{R_0}=\frac{X\times\varepsilon}{2R_1} \quad (3)$$

By fitting the experimental data for 250%-500% strain with green line, as shown in Figure S11b, X and R_2 could be determined to be 27 and 27 (kΩ%)×strain (%), respectively.

For small strain region (under 250% strain for the plain-weave CSF strain sensor), the experimental data within 250% strain could also be fitted as shown in Figure S11 to determine Y and R_c to be 9.3 kΩ and 9.3 (kΩ%)×strain (%), respectively.

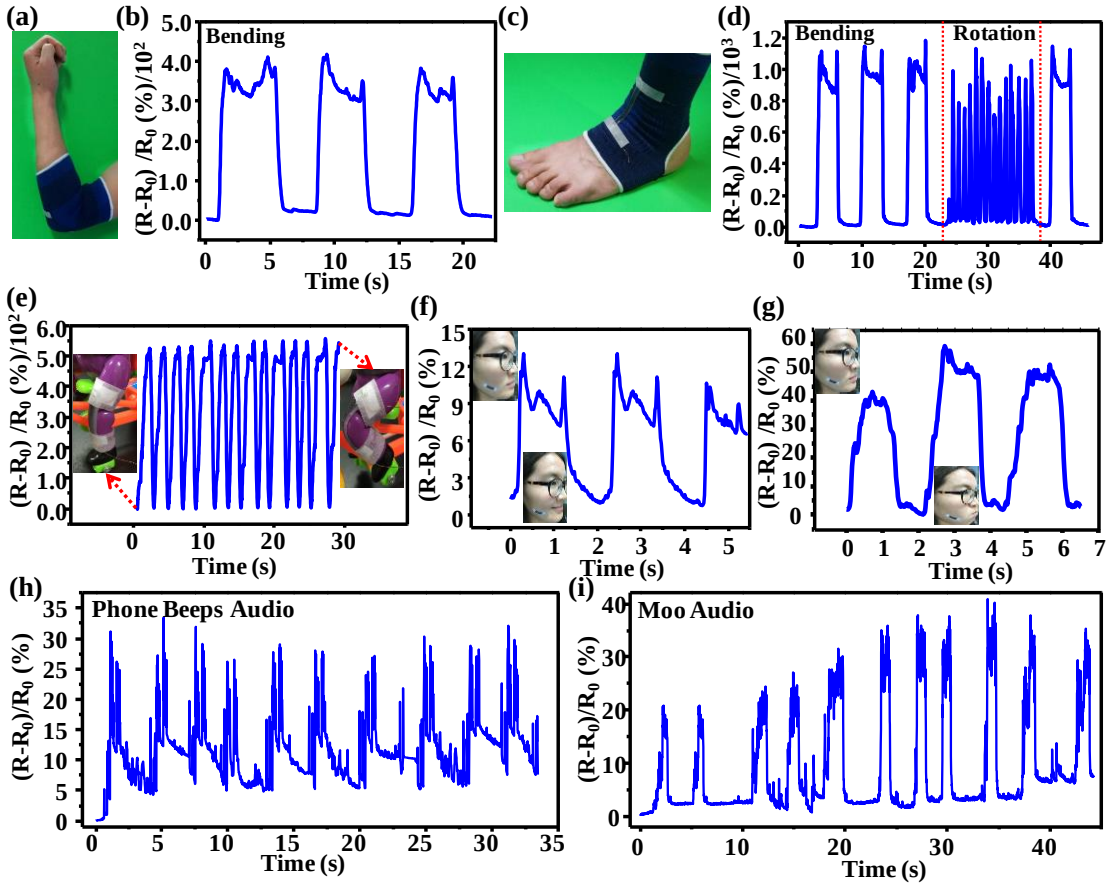

Figure S12. (a) Photograph of a CSF strain sensor attached to an elbow guard. (b) Signals of the sensor in (a) showing the bending of the elbow. (c) Photograph of a CSF strain sensor attached to an ankle guard. (d) Signals of the sensor in (c) showing the bending and rotation of the ankle. (e) Responsive signals of a CSF strain sensor on the knee of a robot during the robot leg cycling. Inset: photographs of knee bending and relaxing. (f, g) Responsive signals of the CSF strain sensor in monitoring tiny muscle movement of smiling (f) and cheek bulging (g). Inset: photographs of poke face and smiling face in (f), poke face and cheek-bulging face in (g). (h, i) Recognition of sound signals using the CSF strain sensor: (h) phone beeps audio and (i) moo audio.

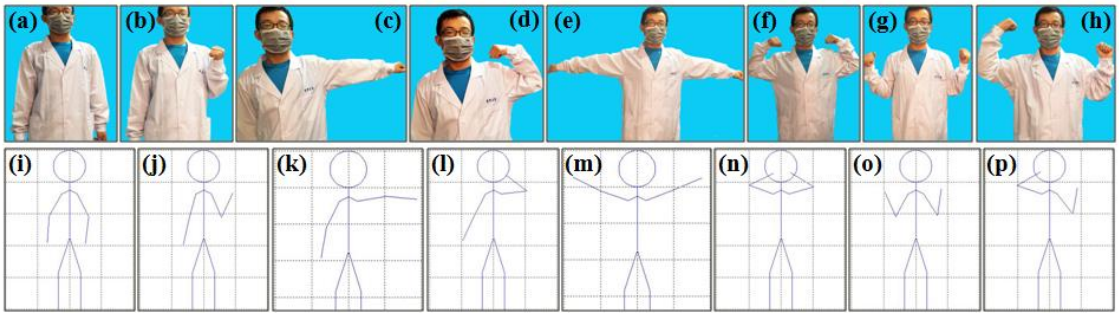

Figure S13. Capture and reconstruction of human body motion using the wearable CSF strain sensors. (a-h) Photographs showing motions of upper limbs. (i-p) The corresponding reconstructed motion images by connecting the motion induced resistance signals of sensors with a computer program.

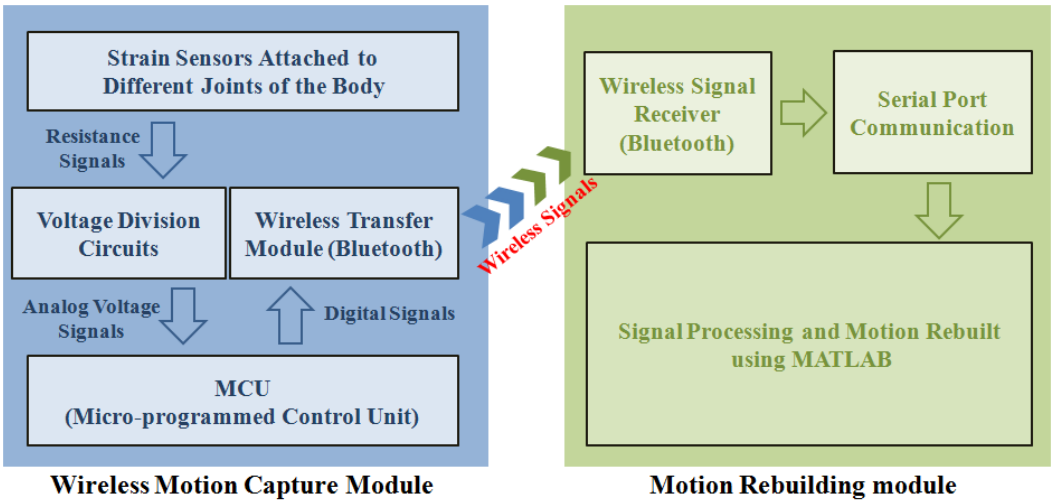

Figure S14. Schematic illustration showing system for the human body motion reconstruction, consisting of wireless motion capture module and motion rebuilding module.

Figure S13 shows the elements of the self-designed motion reconstruction system. In the wireless motion capture module, the circuit board consists of the voltage division circuits, a micro-programmed control unit (MCU) (STC12C5A60S2), and a Bluetooth signal transfer module. The motion induced resistance signals of the strain sensors were transformed to analog voltage signals via the voltage division circuits. The MCU serves as the analog-to-digital converter and signal transmitter. The Bluetooth signal transfer module receives digital signals from the MCU and sends wireless signals to the motion reconstruction module. In the motion reconstruction module, the signals are collected by a Bluetooth receiver and transferred to MATLAB via Serial Port Communication. The motion construction is performed on a computer using MATLAB according to the data received.

References

[1] Y. Cheng, R. Wang, J. Sun, L. Gao, *Adv. Mater.* **2015**, *27*, 7365.

[2] C. S. Boland, U. Khan, C. Backes, A. O'Neill, J. McCauley, S. Duane, R. Shanker, Y. Liu, I. Jurewicz, A. B. Dalton, *ACS nano* **2014**, *8*, 8819.

[3] C. Yan, J. Wang, W. Kang, M. Cui, X. Wang, C. Y. Foo, K. J. Chee, P. S. Lee, *Adv. Mater.* **2014**, *26*, 2022.

[4] S. Ryu, P. Lee, J. B. Chou, R. Xu, R. Zhao, A. J. Hart, S.-G. Kim, *ACS nano* **2015**, *9*, 5929.

[5] T. Yamada, Y. Hayamizu, Y. Yamamoto, Y. Yomogida, A. Izadi-Najafabadi, D. N. Futaba, K. Hata, *Nat. Nanotech.* **2011**, *6*, 296.

[6] C. Mattmann, F. Clemens, G. Tröster, *Sensors* **2008**, *8*, 3719.